Earth, Planets and Space

FULL PAPER Open Access

Behavior of magmatic components in fumarolic gases related to the 2018 phreatic eruption at Ebinokogen Ioyama volcano, Kirishima Volcanic Group, Kyushu, Japan

Takeshi Ohba[1*], Muga Yaguchi[2], Urumu Tsunogai[3], Masanori Ito[3] and Ryo Shingubara[3]

Abstract

Direct sampling and analysis of fumarolic gas was conducted at Ebinokogen Ioyama volcano, Japan, between December 2015 and July 2020. Notable changes in the chemical composition of gases related to volcanic activity included a sharp increase in SO_2 and H_2 concentrations in May 2017 and March 2018. The analyses in March 2018 immediately preceded the April 2018 eruption at Ioyama volcano. The isotopic ratios of H_2O in fumarolic gas revealed the process of formation. Up to 49% high-enthalpy magmatic vapor mixed with 51% of cold local meteoric water to generate coexisting vapor and liquid phases at 100–160 °C. Portions of the vapor and liquid phases were discharged as fumarolic gases and hot spring water, respectively. The CO_2/SO_2 ratio of the fumarolic gas was higher than that estimated for magmatic vapor due to SO_2 hydrolysis during the formation of the vapor phase. When the flux of the magmatic vapor was high, effects of hydrolysis were small resulting in low CO_2/SO_2 ratios in fumarolic gases. The high apparent equilibrium temperature defined for reactions involving SO_2, H_2S, H_2 and H_2O, together with low CO_2/SO_2 and H_2S / SO_2 ratios were regarded to be precursor signals to the phreatic eruption at Ioyama volcano. The apparent equilibrium temperature increased rapidly in May 2017 and March 2018 suggesting an increased flux of magmatic vapor. Between September 2017 and January 2018, the apparent equilibrium temperature was low suggesting the suppression of magmatic vapor flux. During this period, magmatic eruptions took place at Shinmoedake volcano 5 km away from Ioyama volcano. We conclude that magma sealing and transport to Shinmoedake volcano occurred simultaneously in the magma chamber beneath Ioyama volcano.

Keywords: Phreatic eruption, Volcanic gas, Fumarole, Hydrothermal reservoir, Magmatic vapor

Introduction

Although phreatic eruptions are generally small in scale, they can nonetheless cause injuries and fatalities. The phreatic eruption at Ontake Volcano Japan in 2014 killed 58 tourists at the summit area (Oikawa et al. 2016). Prior to the eruption, some volcanic earthquakes had been observed by the Japan Meteorological Agency (JMA); however, the eruption occurred in advance of the announcement of an evacuation advisory to tourists. A skier was also killed by falling rocks ejected during the phreatic eruption of Moto-Shirane Volcano Japan in 2018 (Japan Meteorological Agency 2020a). No precursory volcanic earthquake was observed prior to that eruption.

The detection of volcanic earthquakes is in some cases insufficient to mitigate disasters resulting from phreatic eruptions (Barberi 1992; Stix and de Moor 2018), and it is, thus, necessary to evaluate the eruptive potential of such volcanoes on the medium and long term using methods in addition to seismic observation. Phreatic eruption involves the explosion of hydrothermal fluid

*Correspondence: takeshi_ohba@tokai-u.jp
[1] Tokai University, 4-1-1 Kitakaname Hiratsuka, Kanagawa 259-1291, Japan
Full list of author information is available at the end of the article

reservoirs that develop in the relatively shallow crust. These reservoirs comprise groundwater from aquifers, which absorbs high-enthalpy magmatic vapor (MV). SO_2 and CO_2 are the typical constituent chemical species of MV components. By understanding the behavior of MV, the potential of medium- to long-term phreatic eruptions can be evaluated. Geochemical observations of fumarolic gas could improve our understanding of MV behavior, because such gases dominate the gas phase in hydrothermal reservoirs that leak to the surface (e.g., Ossaka et al., 1980; Taran et al. 2002; Tassi et al. 2003; Chiodini et al. 2010; Fischer et al. 2015; Ohba et al. 2019a, b). In addition to the MV component, fumarolic gases include components formed within the hydrothermal reservoir (HR). Here, HR components are composed of reducing chemical species such as H_2S and CH_4. Those H_2S and CH_4 are thought to be reduced from the magmatic SO_2 and CO_2, respectively, by the Fe^{2+} contained in the crustal rocks contacting with the fluid in hydrothermal reservoir (Giggenbach 1997). The coexistence of MV and HR components in fumarolic gases was identified at White Island, New Zealand (Giggenbach 1987). Before the phreatic eruption at Hakone Volcano in 2015, volcanic earthquakes occurred, and the ratio of MV to HR components increased according to the frequency of earthquakes (Ohba et al. 2019a). Such changes in fumarolic gas can be attributed to the injection of MV into the HR. This injection induces increases in fluid pressure in the HR and may initiate volcanic earthquakes (Ohba et al. 2019a).

From the viewpoint of general volcanic disaster prevention, it is important to investigate MV components in fumarolic gases prior to phreatic eruptions at volcanoes such as Hakone volcano. A phreatic eruption took place in April 2018 at Ebinokogen Ioyama volcano (hereafter "Ioyama volcano") (Tajima et al. 2020). Between December 2015 and July 2020, we repeatedly collected and analyzed fumarolic gases at Ioyama volcano to investigate the behavior of MV components in fumarolic gases before and after the eruption, and to extract geochemical parameters that could be used to denote precursor events in advance of the main eruption.

Geological settings

The Kirishima volcanic group is located near the volcanic front on Kyushu Island Japan (Fig. 1a). Ioyama volcano (Io) is among the volcanoes in this group, and is surrounded by many volcanic craters and cones formed during the Quaternary period (Fig. 1b). The formation ages

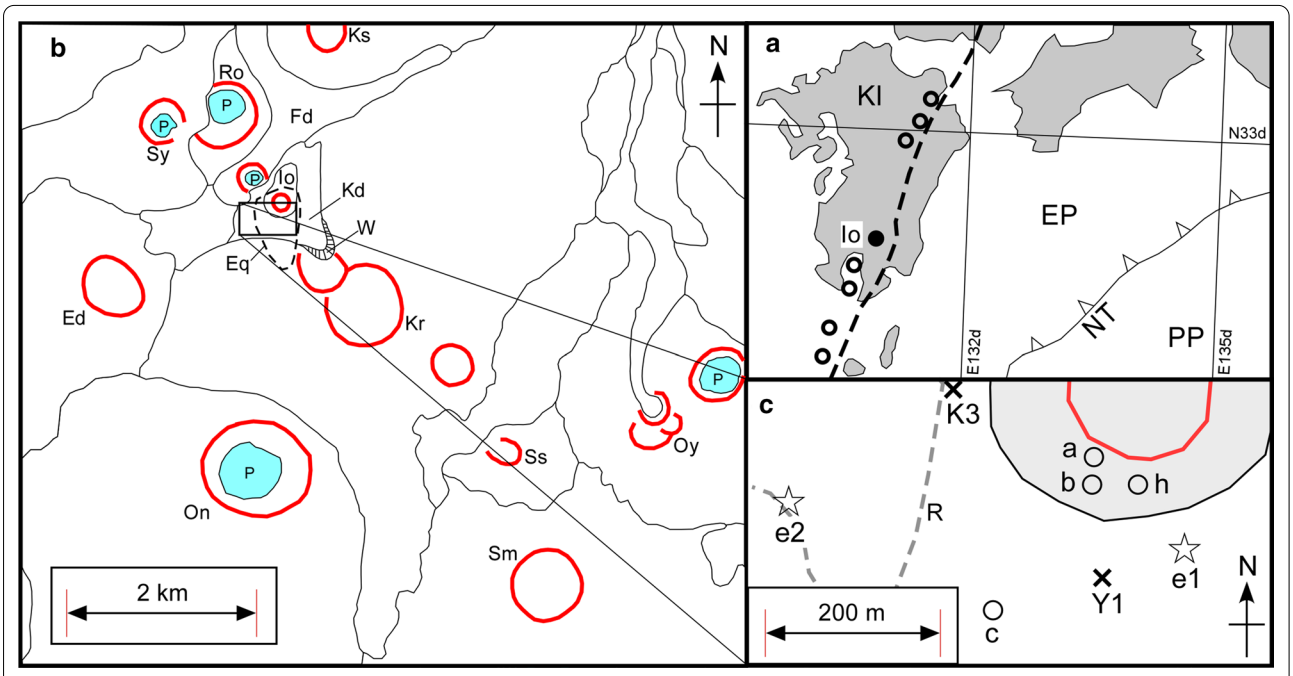

Fig. 1 **a** Location of Ebinokogen Ioyama volcano (Io) on Kyushu Island (KI), Japan. The Philippine Sea Plate (PP) is subducting beneath the Eurasian Plate (EP) on which KI is situated. PP and EP are separated by the Nankai trough (NT). Circles and broken line indicate active volcanoes and the volcanic front, respectively. **b** Io surrounded by Ebinodake volcano (Ed), Karakunidake volcano (Kr), Shiratori-yama crater (Sy), Rokkannonmiike crater (Ro), and Fudoike crater (Fd). Kd is a debris avalanche deposit. P and W denote ponds and collapse walls, respectively. Eq denotes the region in which the volcanic earthquake hypocenters are distributed. Sm, Ss, Oy, Ks and On denote Shinmoedake volcano, Shishidodake volcano, Ohatayama volcano, Koshikidake volcano and Onamiike volcano, respectively. Bold red curves indicate the crater rim. **c** Location of fumaroles a, b, c and h. Phreatic eruptions took place at e1 and e2 on April 16 and 26, 2018, respectively. Hot spring water was discharged at K3 and Y1. R denotes roads

of Ebinodake volcano (Ed), Karakunidake volcano (Kr), Shiratori-yama crater (Sy), Rokkannonmiike crater (Ro) and Fudoike crater (Fd) were estimated to be 70–300 ka, 15 ka, 18–25 ka, 25 ka, and 6.3 ka, respectively (Imura and Kobayashi 2001). A part of northwest flank of Kr has collapsed and spread a debris avalanche deposit (Kd). The andesitic Ioyama volcanic body was developed on Kd during a magmatic eruption in 1768 (Imura and Kobayashi 2001). During January 2011, subplinian eruptions (VEI = 3) occurred at Shinmoedake volcano (Nakada et al. 2013), which is located 5 km southeast of Ioyama volcano. Following the 2011 events, magmatic eruptions took place at Shinmoedake volcano in October 2017, March 2018 and April 2018. Prior to the 2017 eruption, crustal deformation was observed in the area of the Kirishima volcano group (Japan Meteorological Agency 2020b). This deformation was interpreted to result from the combination of shrinking beneath Ioyama volcano and inflation beneath Shinmoedake volcano, suggesting that the magma transport had occurred from a magma chamber beneath Ioyama volcano to Shinmoedake volcano.

To clarify the magma plumbing system of the Kirishima volcanoes, a magnetotelluric (MT) survey was conducted (Utada et al. 1994). Based on the one-dimensional (1D) analysis of these results, the emplacement of a magma chamber was suggested at − 10 km from the surface (Utada et al. 1994). A low-resistivity region was also detected approximately 5 km beneath Ioyama volcano, which was interpreted to be a small magma chamber or magmatic gas reservoir. Three-dimensional (3D) analyses of these MT survey data confirmed the depth of magma chamber at − 10 km depth, located 10 km west of Ioyama volcano as shown schematically in Fig. 2 (Aizawa et al. 2014). These analyses also detected a vertical electric conductor beneath Ioyama volcano, which was interpreted to be a magmatic vapor reservoir zone (MVR in Fig. 2) with temperatures greater than 400 °C. This vertical conductor extends between − 5 and − 3 km, and was estimated to be a magma pathway that was partially

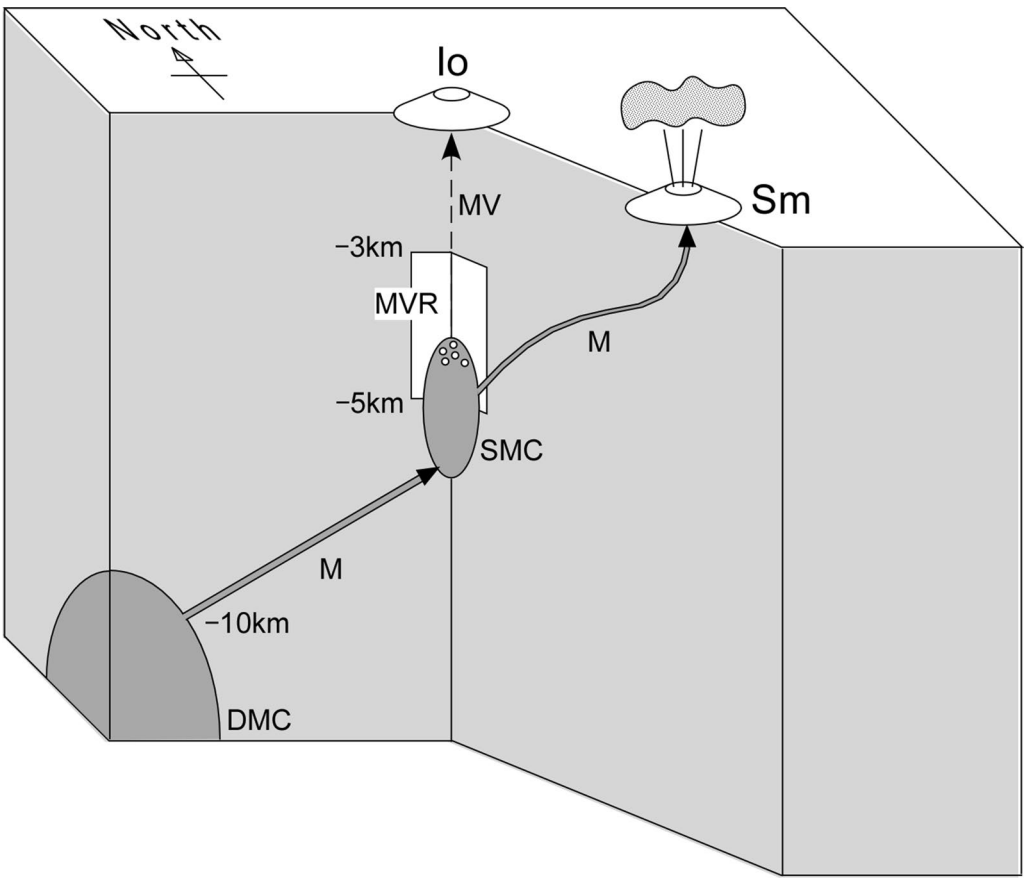

Fig. 2 Schematic illustration of the magma plumbing system revealed by a previous 3D-MT survey (Aizawa et al. 2014). MV and M refers to magmatic vapor and magma, respectively. Io and Sm denote the Ioyama and Shinmoedake volcanoes, respectively. MVR, SMC and DMC are the magmatic vapor reservoir, shallow magma chamber and deep magma chamber, respectively

formed before magmatic eruptions at Shinmoedake volcano (Aizawa et al. 2014).

An area of active fumarolic activity has been observed around the summit of Ioyama volcano since the early of 1900s (Funasaki et al. 2017). During the 1970s, the fumarolic activity was particularly intense, and the temperature of fumarolic gases reached 247 °C (Kagiyama et al. 1979). In 1994, the temperature of fumarolic gas decreased to 101 °C (Ohba et al. 1997), and after the 1990s, the fumarolic activity gradually decreased. After 2007 the discharge of fumarolic gas around the summit area of Ioyama volcano ceased completely (Funasaki et al. 2017), and the seismic activity has been continually low (Japan Meteorological Agency 2020b).

Since mid-2015, however, volcanic earthquakes have been observed sporadically. In December 2015, fumarolic gas discharge was confirmed to occur for the first time since 2007 (position a, Fig. 1c). Since December 2015, fumarolic gas emissions at Ioyama volcano have become increasingly intense. Tajima et al (2020) reported superficial phenomena occurring at Ioyama volcano in details from 2015 to 2018. According to their report, the geothermal surface area with temperatures higher than 50 °C was approximately 2000 m^2 in May 2016. This geothermal area gradually increased to around 10,000 m^2 in June 2017. In May 2017, a strong fumarole characterized by a roaring sound developed (position h, Fig. 1c). Following the appearance of this fumarole, the geothermal surface area temporarily decreased to about 4000 m^2 in October 2017. This reduced geothermal area was maintained until around February 2018, at which time the number of earthquakes increased sharply. On April 19 and 26, 2018, phreatic eruptions occurred (positions e1 and e2 in Fig. 1c, respectively). The eruption on April 19 2018 began at 15:39 and lasted for about 15 h, and the height of the eruption column was about 500 m at maximum (Japan Meteorological Agency 2020b). The total volume of the ejecta was estimated to be 1500 m^3, and no juvenile materials were detected in the ejecta (Tajima et al 2020).

Volcanic earthquakes on Ioyama volcano were observed to occur mostly below the summit crater and in the area extending to the south (Fig. 1b). The depth of their epicenters was distributed in the range of − 3 to − 1 km below sea level (Japan Meteorological Agency 2020b). According to Tajima et al (2020), the shallow crust beneath Ioyama volcano is estimated to have the following layers.

Layer-1: Vadose zone (− 50 m from the surface);

Layer-2: Aquifer (the groundwater layer);

Layer-3: Low-temperature hydrothermal layer (the groundwater mixed with hydrothermal fluid at temperatures less than 200 °C);

Layer-4: Impermeable layer (caprock);

Layer-5: Hydrothermal reservoir (at depths greater than − 600 m from the surface and temperatures is higher than 200 °C).

Volcanic earthquakes at Ioyama volcano occurred mostly in Layer-5. The point in Layer-5 just below the summit crater was a pressure source of crustal deformation since July 2017 (Japan Meteorological Agency 2020b).

Sampling and analysis of fumarolic gases

Fumarolic gases were repeatedly sampled at positions a, b and c (see Fig. 1c). Samplings were obtained at 17 occasions between December 2015 and July 2020. In addition to the above three fumaroles, one fumarolic gases was sampled at position h in July 2020 (Fig. 1c). The outlet temperature of fumarolic gas was measured using a thermocouple with a K-type sensor (Yokogawa Electric Corp., TX-10). Fumarolic gas was introduced using a titanium pipe inserted directly into the fumaroles from which samples were obtained. The end of the titanium pipe was connected to a rubber tube, which was in turn connected to a 120 ml pre-evacuated Pyrex glass bottle with an airtight stop cock (Giggenbach 1975), where 20 ml of 5 M KOH solution was introduced. Water vapor and acidic gases (CO_2, SO_2, H_2S, etc.) were absorbed by the KOH solution whereas the residual gases (hereafter R-gas), e.g., N_2, O_2, Ar, He, H_2, and CH_4 were maintained in the headspace of the glass bottle. The chemical species in the KOH solution were analyzed according to the methods of Ozawa (1968). The H_2S/SO_2 ratio in the fumarolic gas was determined using a KI–KIO_3 solution (Lee et al. 2016) and the total molar amount of R-gas was determined by the head space volume of the bottle and the inner pressure of the head space at room temperature. Based on the molar amount of H_2O, CO_2, H_2S, SO_2 and R-gas, the relative concentration (ppm) of each gas was calculated (Table 1). The analysis of R-gas by gas chromatography followed the methods of Ohba et al. (2019a, b).

For isotopic analysis of water vapor in fumarolic gas, this gas was cooled using a double-tube condenser made of Pyrex glass. The isotopic ratio of the condensed water was determined using an IR-laser cavity ring down analyzer (Picarro Inc., L2120-i). The analytical precision of the analyzer was ± 0.12‰ and ± 0.05‰ for δD and $\delta^{18}O$, respectively. The isotopic ratio of H_2 in the R-gas was determined using a continuous flow system combined with a mass spectrometer (Thermo Fischer Scientific Delta V) (Tsunogai et al. 2011). The analytical precision of the analyzer was ± 0.8‰ for δD of H_2.

Table 1 Concentration of chemical species in fumarolic gases and isotopic ratio of H_2O and H_2 with their corresponding apparent equilibrium temperatures (AETS and AETD). The unit of concentration is in micro-mol/mol (= ppm)

Location	Date, mm/dd/yyyy	Temp, ℃	H_2O	CO_2	H_2S	SO_2	He	H_2	O_2	N_2	CH_4	Ar	H_2O, δD_{SMOW} ‰	H_2O, $\delta^{18}O_{SMOW}$ ‰	H_2, δD_{SMOW} ‰	AETS, ℃	AETD, ℃
a	12/22/2015	97.2	984,285	14,163	1192	26.8	0.209	1.73	0.145	328	0.401	2.65	− 91	− 14.1	− 400	232	385
a	2/24/2016	97.2	982,088	16,532	1037	84.7	0.232	7.40	0.091	250	0.211	1.09	− 52	− 6.3	− 229	313	726
a	5/6/2016	95.3	978,065	20,210	1459	58.5	0.192	4.30	0.050	201	0.206	1.91	− 57	− 6.6	− 348	277	437
a	8/30/2016	96.9	982,596	14,237	2977	48.9	0.122	8.77	0.093	131	0.165	0.47	− 41	− 5.3	− 464	296	252
a	1/17/2017	96.4	991,615	6493	1756	67.3	0.043	15.4	0.022	53	0.060	0.21	− 43	− 3.6	− 284	338	549
a	5/15/2017	96.5	988,363	6601	2177	2303	0.055	468	0.000	89	0.088	0.26	− 42	− 2.2	− 173	752	926
a	9/15/2017	106.0	991,168	5444	3077	215	0.055	24.1	0.012	71	0.077	0.42	− 48	− 3.7	− 354	376	416
a	10/18/2017	96.0	989,645	8683	1418	149	0.070	20.4	0.475	84	0.055	0.35	− 48	− 3.5	− 204	374	804
a	11/28/2017	95.9	990,814	6954	1965	103	0.080	49.1	0.044	114	0.076	0.49	− 49	− 3.7	− 436	416	292
a	1/26/2018	96.8	988,768	7798	3227	77.5	0.076	27.2	0.075	102	0.045	0.55	− 48	− 3.7	− 141	361	1152
a	3/28/2018	96.2	984,731	9104	2993	2901	0.098	166	0.369	104	0.064	0.36	− 46	− 2.2	− 120	611	1310
a	5/29/2018	96.7	996,200	2867	367	421	0.026	110	0.048	34	0.020	0.21	− 45	− 2.4	− 141	571	1127
a	10/19/2018	95.6	983,165	15,786	822	42.2	0.127	22.6	0.070	162	0.122	0.62	− 69	− 8.1	− 385	366	385
a	1/25/2019	96.1	994,356	4894	508	103	0.038	19.6	2.97	115	0.046	1.02	− 64	− 6.7	− 402	385	353
a	5/31/2019	96.0	993,015	5915	850	28.9	0.077	8.45	0.110	181	0.034	1.50	− 84	− 11.7	− 471	305	272
a	11/8/2019	94.1	943,027	9299	1276	419	0.267	11.1	1187	44,213	–	568	− 93	− 14.6	− 565	363	171
a	2/14/2020	93.6	735,078	43,125	10,430	889	0.924	24.7	29,985	177,916	–	2552	− 89	− 14.3	− 484	400	261
a	7/31/2020	88.1	–	–	–	–	–	–	–	–	–	–	− 94	− 15.9	–	–	–
b	2/24/2016	96.2	982,869	15,845	960	42.5	0.217	7.04	0.155	275	0.183	1.58	− 78	− 11.9	− 242	301	756
b	5/6/2016	95.2	973,056	24,918	1717	50.6	0.239	5.48	0.092	251	0.261	1.92	− 67	− 9.2	− 355	283	437
b	8/30/2016	95.2	974,618	20,773	4329	55.0	0.191	13.8	0.116	210	0.277	0.82	− 56	− 7.5	− 468	314	256
b	1/17/2017	97.0	992,873	5462	1596	18.8	0.040	4.24	0.040	46	0.054	0.17	− 46	− 4.6	− 611	258	110
b	5/15/2017	96.6	989,119	7887	1575	680	0.103	603	0.000	135	0.157	0.34	− 46	− 4.0	− 399	745	340
b	9/15/2017	96.4	993,226	4017	2622	42.6	0.046	27.0	0.052	65	0.074	0.37	− 44	− 1.9	− 457	353	262
b	10/18/2017	96.0	990,369	8208	1270	45.3	0.076	18.4	0.066	89	0.044	0.31	− 45	− 2.6	− 199	347	817
b	11/28/2017	96.0	985,348	11,939	2455	32.6	0.130	44.5	0.076	179	0.106	0.84	− 47	− 3.4	− 506	380	208
b	1/26/2018	96.4	990,910	6373	2588	8.3	0.073	16.6	0.059	103	0.049	0.59	− 44	− 1.9	− 271	300	584
b	3/28/2018	97.7	992,249	6145	565	863	0.070	107	0.056	70	0.072	0.21	− 40	− 1.3	− 178	579	891
b	10/19/2018	96.8	984,067	15,061	655	56.1	0.118	17.7	0.328	143	0.109	0.47	− 51	− 3.8	− 430	361	301
b	1/25/2019	95.0	992,940	6279	540	146	0.049	23.5	0.166	70	0.045	0.31	− 46	− 2.6	− 391	403	352
b	5/31/2019	96.0	994,446	4735	653	29.0	0.059	5.81	0.034	130	0.046	0.96	− 60	− 6.0	− 446	291	288
b	2/14/2020	95.8	991,959	7136	754	56.9	0.059	7.73	0.179	85	0.066	0.39	− 78	− 11.2	− 398	314	373
c	5/15/2017	95.2	990,014	7988	1078	367	0.114	416	0.000	135	0.140	0.42	− 57	− 6.8	− 321	681	490
c	9/15/2017	96.1	994,811	2997	2105	15.2	0.042	11.42	0.019	59	0.066	0.37	− 44	− 2.7	− 426	295	301

Table 1 (continued)

Location	Date, mm/dd/yyyy	Temp, ℃	H_2O	CO_2	H_2S	SO_2	He	H_2	O_2	N_2	CH_4	Ar	H_2O, δD_{SMOW} ‰	H_2O, $\delta^{18}O_{SMOW}$ ‰	H_2, δD_{SMOW} ‰	AETS, ℃	AETD, ℃
c	10/18/2017	96.2	989,576	8984	1305	19.8	0.075	3.14	0.026	111	0.057	0.67	− 48	− 3.7	− 469	250	250
c	11/28/2017	95.8	985,615	11,639	2511	39.7	0.132	5.16	0.076	189	0.144	0.90	− 51	− 4.5	− 586	271	133
c	1/26/2018	95.7	990,153	7152	2557	19.6	0.079	4.52	0.063	113	0.039	0.64	− 44	− 2.7	− 534	255	178
c	3/28/2018	97.0	991,404	7370	609	420	0.081	108	0.139	89	0.101	0.32	− 46	− 3.3	− 239	552	677
c	5/29/2018	96.1	990,254	8215	1367	41.4	0.062	16.0	0.034	105	0.069	0.98	− 50	− 4.1	− 433	336	296
c	10/19/2018	94.8	944,418	52,031	2874	18.3	0.545	3.23	0.380	649	0.674	3.59	− 73	− 10.3	− 626	241	107
c	1/25/2019	97.6	973,434	23,782	2555	17.3	0.164	3.52	0.103	206	0.248	1.22	− 65	− 8.5	− 613	244	115
c	5/31/2019	94.7	984,364	12,479	2840	23.9	0.169	5.46	0.035	284	0.307	2.90	− 80	− 12.7	− 615	264	118
c	11/8/2019	94.0	732,980	160,775	19,146	251	1.53	21.2	14,915	71,048	3.41	859	− 93	− 16.0	− 627	353	112
c	2/14/2020	93.5	861,783	128,932	6955	69.8	1.81	6.71	2.32	2240	1.65	7.54	− 82	− 13.9	− 635	282	102
c	7/31/2020	85.9	422,263	542,741	24,290	201	5.44	13.2	32.6	10,337	8.66	108	− 99	− 18.0	− 653	348	92
h	7/31/2020	95.9	995,551	3785	183	357	0.034	6.20	8.08	109	0.00	0.98	− 78	− 14.2	− 346	360	471

Results

Table 1 lists the data obtained on fumarolic gas, including outlet temperature, chemical composition, isotopic ratios (δD and $\delta^{18}O$) of H_2O and the isotopic ratios (δD) of H_2. The outlet temperatures were predominantly close to the boiling point (95.8 °C) of water under standard air pressures at the altitude of the fumaroles (1300 m) (Fig. 3a). The outlet temperature of fumarole "a" was 106 °C in September 2017, 10 °C higher than the boiling temperature. The outlet temperatures of fumaroles a and c have dropped significantly below their boiling point since November 2019. The histograms in Fig. 3a, b indicate the number of earthquakes observed monthly by the JMA. Vertical lines indicate the phreatic eruption of Ioyama volcano (April 19, 2018) and the magmatic eruptions at Shinmoedake volcano (October 11, 2017, March 1, 2018, and April 5, 2018). The fumarolic gases were mostly dominated by H_2O vapor, except the fumaroles a and c after November 2019 (Fig. 3b). Figure 4 shows temporal changes in the logarithmic concentrations (ppm) of CO_2, H_2S, SO_2, He, H_2, O_2, N_2, CH_4, and Ar. After November 2019, the concentrations of N_2, O_2, and Ar in fumaroles a and c increased significantly, indicating air contamination. The SO_2 and H_2 concentration of fumaroles a, b, and c increased significantly during May 2017 and March 2018 (Fig. 4c, e).

In the following, we divide the observation period based on the isotopic ratio of H_2O (Fig. 5a, b).

Period- I: December 2015 to December 2016;

Period- II: January 2017 to May 2018;

Period- III: June 2018 to July 2020.

During Period-1, δD increased from approximately − 90‰ to the around of − 50 ~ − 40‰, while the $\delta^{18}O$ increased from about − 14‰ to the range of − 4 ~ − 1‰ (Fig. 5a, b). The number of earthquakes during this period was relatively small, and the activity of Ioyama volcano is regarded to be in its preparatory stage.

During Period-II, the δD and $\delta^{18}O$ maintained relatively high values. The highest values of δD and $\delta^{18}O$ were recorded at fumarole b in March 2018 (Fig. 5a, b). Throughout this period, the volcanic activity was enhanced. Shinmoedake volcano exhibited three magmatic eruptions, and phreatic eruptions occurred at Ioyama volcano. More earthquakes occurred in Period-II than in Period-I.

In Period-III, the δD decreased to − 100‰ and the $\delta^{18}O$ decreased to − 18‰. The number of earthquakes was high at the beginning of this period but gradually decreased. No eruptions occurred in this period at Ioyama volcano.

For the δD of H_2, the highest values were recorded at fumarole "a" in March 2018 (Fig. 5c). In terms of the δD of H_2, the time variation at the three fumaroles did

not harmonize. For example, considering the changes between August 2016 and January 2017, the δD at fumarole "a" increased significantly, while that at fumarole b decreased. The δD at fumarole c was low between October 2018 and July 2020, whereas the δD of fumarole b was 200‰ higher than that of fumarole c for the same period. The three fumaroles are located close to one another (Fig. 1c); thus, their distinct δD implies that the phenomena controlling the δD of H_2 operated at a shallow depth. If δD of H_2 was fixed at a large depth, the δD is expected to be similar for fumaroles located close each other.

The $\delta^{18}O$ and δD values of H_2O in fumarolic gas exhibit a linear distribution (Fig. 5d). K3 and Y1 are hot spring waters collected at Ioyama volcano (Tajima et al 2020); collection locations are shown in Fig. 1c. K3 represents local meteoric water (Tajima et al. 2020). Y1 is a hot spring water discharging near the eruptive point e1 (Fig. 1c), which appeared just before the phreatic eruption of Ioyama volcano, with a temperature on April 16, 2018 of 93 °C (Tajima et al. 2020). AMW is general isotopic composition of H_2O degassed from andesitic magma (Taran et al. 1989; Giggenbach 1992). Some fumarolic gas samples are distributed near the lines connecting AMW and K3, but most are distributed in the area below these lines, suggesting that a simple mixing model between the local meteoric water and AMW is insufficient to explain the isotopic ratio of H_2O in fumarolic gas.

Discussion

Temporal change of apparent equilibrium temperatures (AETs)

The apparent equilibrium temperature based on sulfur species in fumarolic gas (hereafter AETS) is defined in terms of the following reaction (e.g., Ohba et al 1994):

$$SO_2 + 3H_2 = H_2S + 2H_2O \tag{1}$$

Assuming the equilibrium of reaction as follows:

$$\log K + \log f_{H_2O} = -\log\left(\frac{SO_2}{H_2O}\right) - 3\log\left(\frac{H_2}{H_2O}\right) + \log\left(\frac{H_2S}{H_2O}\right) \tag{2}$$

where K and f_{H2O} are, respectively, the equilibrium constant of reaction (1) and the fugacity of H_2O, both of which are functions of temperature. The fractions in parentheses on the right-hand side of Eq. (2) refer to the molar ratio of each gas species relative to H_2O. Based on the temperature dependence of the standard equilibrium constants of formation of elements and the fugacity of H_2O in hydrothermal systems (Giggenbach 1987), the left-hand side (LHS) of Eq. (2) is calculated to be as follows:

$$\mathrm{LHS} = 8924\left(T^{-1}\right) + 1.242 \tag{3}$$

where T is temperature in Kelvin. AETS is defined as the temperature that satisfies Eq. (3).

It is useful to consider AETS because it is the qualitative parameter depending on conditions favoring the retrograde reaction in terms of reaction (1). During the transport of MV from the source to surface, the temperature decreases along the temperature profile of the passage. When the magmatic vapor rises rapidly, the chemical composition of magmatic vapor will be quenched at high temperature without a large change, then, a high AETS is calculated for the fumarolic gas composition. When the magmatic vapor rises slowly, the chemical composition of magmatic vapor will be quenched with a large change because an enough time is allowed to occur reactions at lower temperature among gas species or reactions between gas species and crustal rock, a low AETS is calculated for the fumarolic gas composition (Giggenbach 1987). Therefore, an increase in AETS is often observed during periods of enhanced volcanic activity (e.g., Ohba et al 2011). Another apparent equilibrium temperature (AETD) is defined in terms of the following reaction:

$$HD + H_2O = H_2 + HDO \tag{4}$$

Assuming equilibrium in reaction (4), we obtain the equation of Richet et al (1977):

$$\mathrm{AETD} = \left(4.474 \times 10^{-12}x^2 + 3.482 \times 10^{-9}x + 9.007 \times 10^{-8}\right)^{-\frac{1}{2}} - 273.15 \tag{5}$$

where AETD is in degree C and x is given by

$$x = 1000 \ln\left(\frac{\delta D(H_2O) + 1000}{\delta D(H_2) + 1000}\right) \tag{6}$$

AETS and AETD were high in Period-II relative to Periods-I and -II (Fig. 6a, b). For example, the AETS in May 2017 were 752, 745, and 681 °C at fumaroles a, b, and c, respectively and the AETD in May 2017 was 926, 340, and 490 °C at fumaroles a, b, and c, respectively. Although the AETS at fumaroles a, b and c often show close values, the AETD of fumaroles a, b and c occasionally show large differences due to the correspondingly large differences in the δD of H_2. Therefore, to estimate the qualitative velocity and flux of MV, changes in AETS are more reliable than AETD.

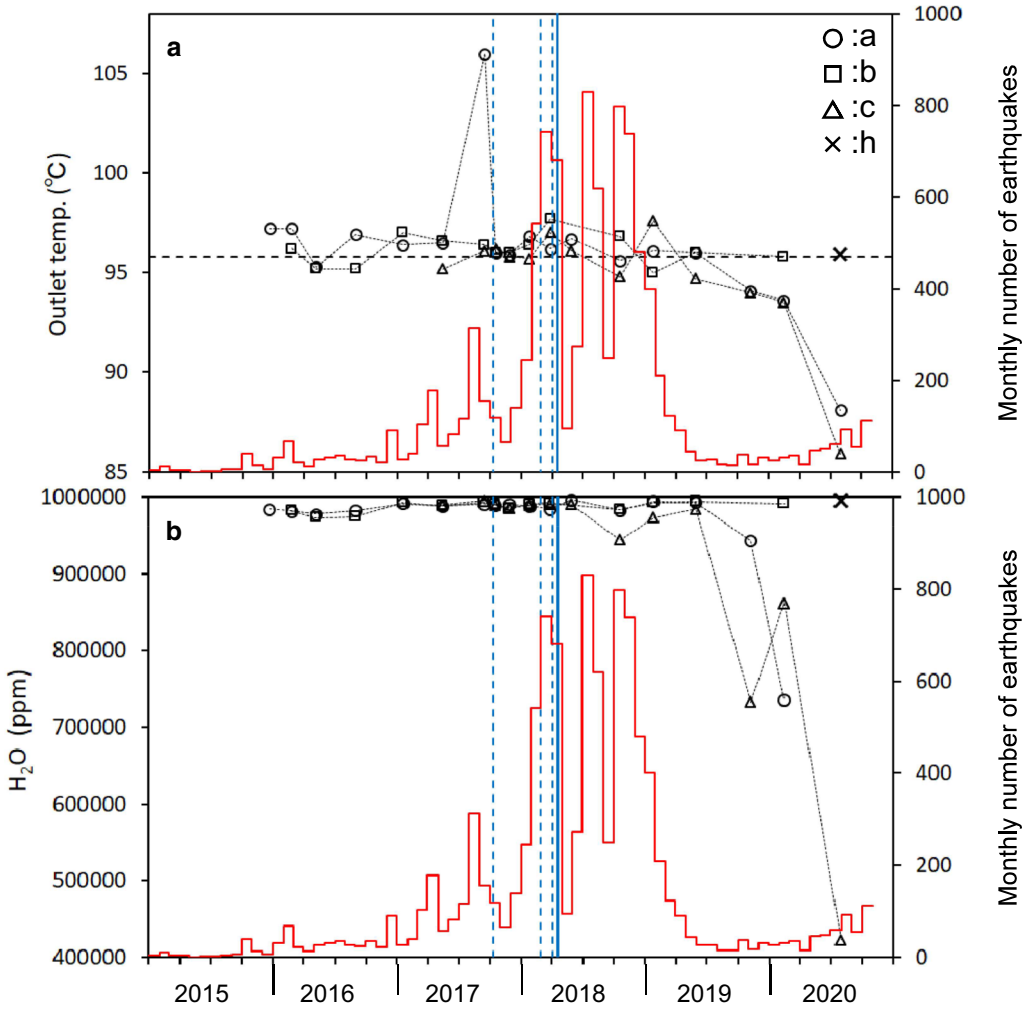

Fig. 3 **a** Changes in fumarolic gas outlet temperature. The horizontal broken line indicates the boiling temperature of water at fumarole altitude. **b** Changes in the H_2O concentration of fumarolic gas. The red histograms in (**a**) and (**b**) indicate the monthly number of volcanic earthquakes observed by the JMA. The blue vertical solid line indicates the eruption at Ioyama volcano and blue vertical broken lines indicate eruptions at Shinmoedake volcano

Behavior of MV

The behavior of MV during Period-II can be estimated by correlating changes in AETS with the eruptive events occurring at Shinmoedake and Ioyama volcanoes (Fig. 7). AETS increased significantly during May 2017, when a strong fumarole appeared at point h. No eruptions occurred at Shinmoedake volcano in May 2017. Consequently, it is estimated that a stagnant magma in the shallow magma chamber (SMC) released a large flux of MV (Fig. 7a). This increased flux shortened the residence time of MV, increasing the value of AETS. Such an increase in MV flux is supported by the enlarged geothermal area observed during this time (Tajima et al. 2020), which reached its maximum in June 2017. The AETS was low between September 2017 and January 2018, suggesting a decrease in MV flux (Fig. 7b). The simultaneous observed reduction in geothermal area (Tajima et al. 2020) is consistent with a decreased MV flux. During the period of low AETS, a magmatic eruption occurred in October 2017 at Shinmoedake volcano, suggesting that magma was transported from the SMC to Shinmoedake volcano. The decreased flux of MV may be explained by magma sealing (Fournier 1999). The number of earthquakes increased from January to March 2018 (Fig. 7c). Furthermore, AETS rose in March 2018. Multiple eruptions occurred at Shinmoedake volcano during this period, and it is, thus, highly probable that SMC discharged magma toward Shinmoedake volcano, and the flux of MV to Ioyama volcano increased simultaneously. Magma movement and the increased MV flux likely occurred due to

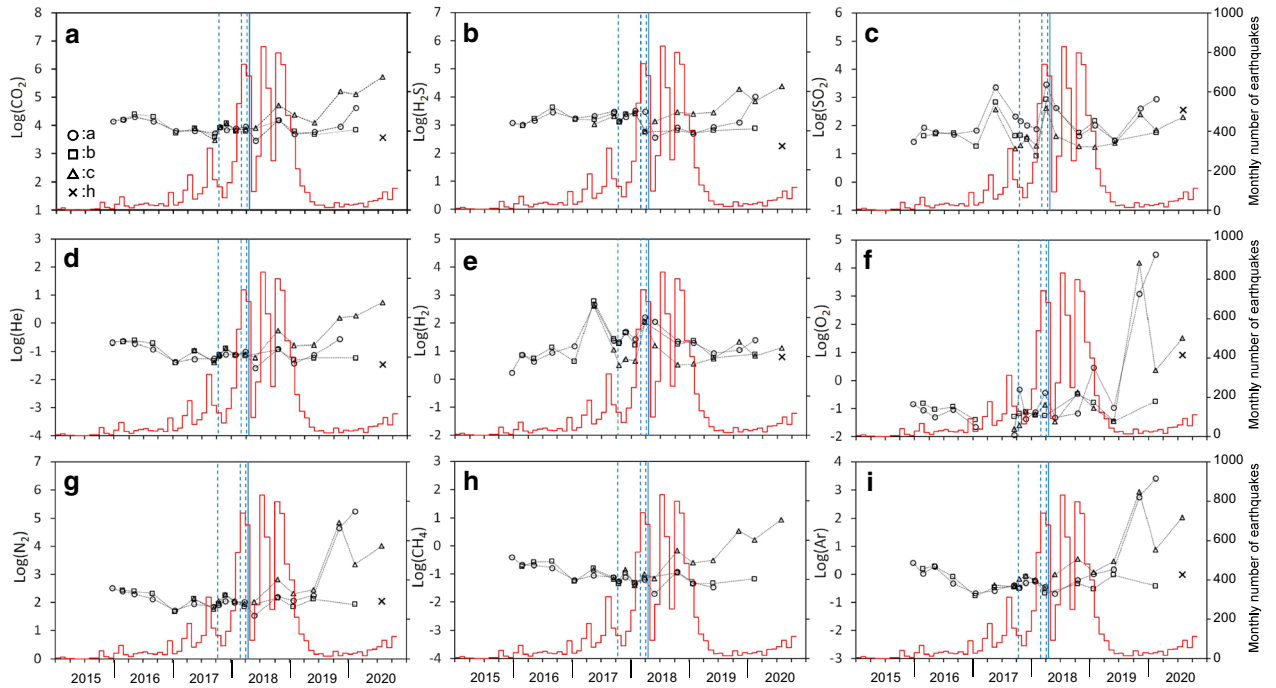

Fig. 4 Changes in the concentration of CO_2 (**a**), H_2S (**b**), SO_2 (**c**), He (**d**), H_2 (**e**), O_2 (**f**), N_2 (**g**), CH_4 (**h**), and Ar (**i**). The vertical axis is calibrated as the logarithm of ppm (μmol/mol) concentration. Red histogram and vertical lines have the same significance as in Fig. 3

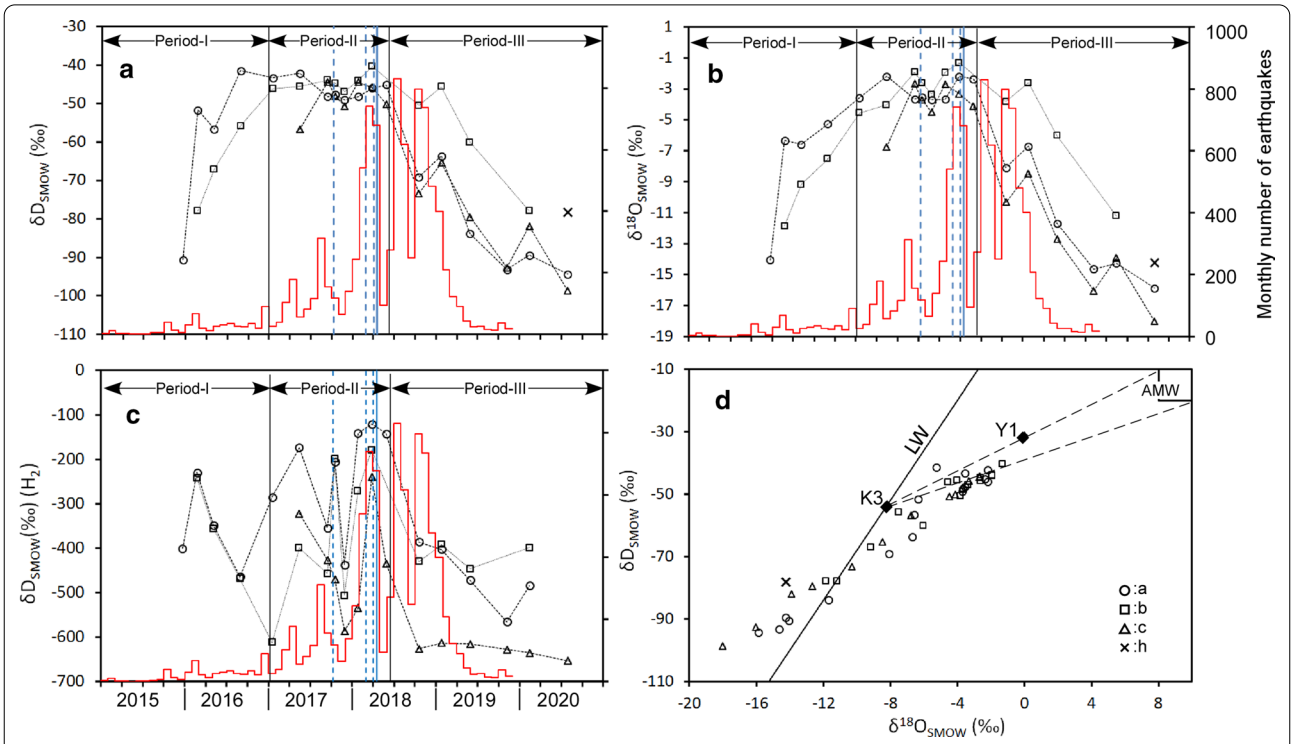

Fig. 5 **a** Changes in the hydrogen isotopic ratio (δD) of H_2O. Red histogram and vertical lines have the same meaning as in Fig. 3. **b** Changes in the oxygen isotopic ratio ($\delta^{18}O$) of H_2O. **c** Changes in the hydrogen isotopic ratio (δD) of H_2. **d** δD and $\delta^{18}O$ of H_2O in fumarolic gas. AMW denotes the general region of magmatic water emitted from andesitic magma. K3 denotes the isotope ratio of local meteoric water. Broken lines show the simple mixing relationship between AMW and K3. LW denotes the local meteoric water line

a volatile enriched magma supply from the deep magma chamber (DMC) to the SMC (Fig. 7c).

Model for the formation of vapor and liquid phases

The correlation between δD and $\delta^{18}O$ of H_2O in the fumarolic gases at the Hakone and Kusatsu-Shirane volcanoes has been explained by the mixing of high-temperature MV and cold local meteoric water (LW), followed by a single-step phase separation (Ohba et al 2019a, b). The concept of this model is illustrated in Fig. 8. Herein, we aim to apply the same model. Assuming enthalpy conservation, the conservation of isotopic ratios, the equilibrium distribution of isotopes between the vapor phase (Vp) and liquid phase (Lp), and the Ar distribution between Lp and Vp, the following equations can be written:

$$H_{MV}f + H_{LW}(1-f) = H_{Vp}g + H_{Lp}(1-g) \tag{7}$$

$$\delta_{MV}f + \delta_{LW}(1-f) = \delta_{Vp}g + \delta_{Lp}(1-g) \tag{8}$$

$$C_{MV}f + C_{LW}(1-f) = C_{Vp}g + C_{Lp}(1-g) \tag{9}$$

$$\alpha = \frac{\delta_{Lp} + 1000}{\delta_{Vp} + 1000} \tag{10}$$

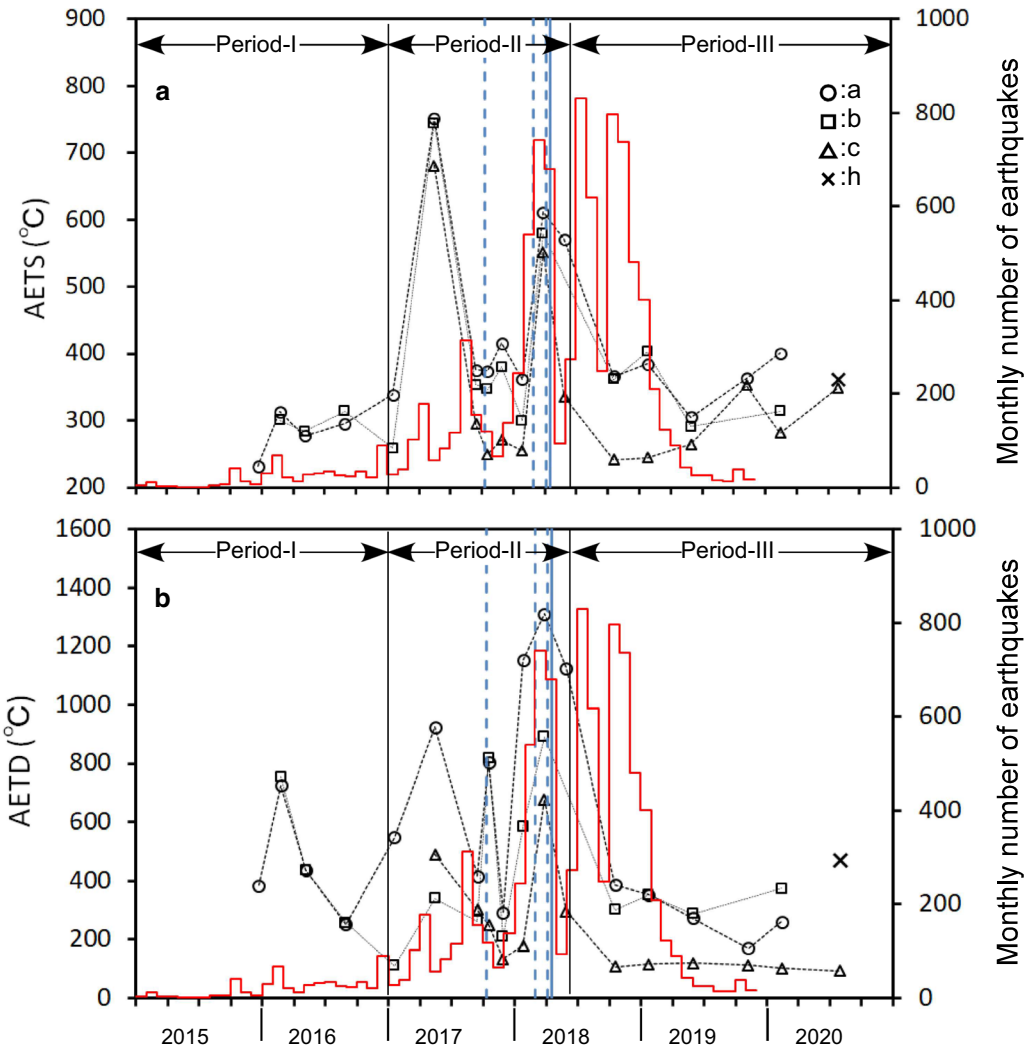

Fig. 6 **a** Changes in the apparent equilibrium temperature (AETS) defined for the reaction involving SO_2, H_2, H_2S and H_2O. **b** Changes in the apparent equilibrium temperature (AETD) defined for the deuterium exchange reaction between H_2O and H_2. Red histogram and vertical lines have the same meaning as in Fig. 3

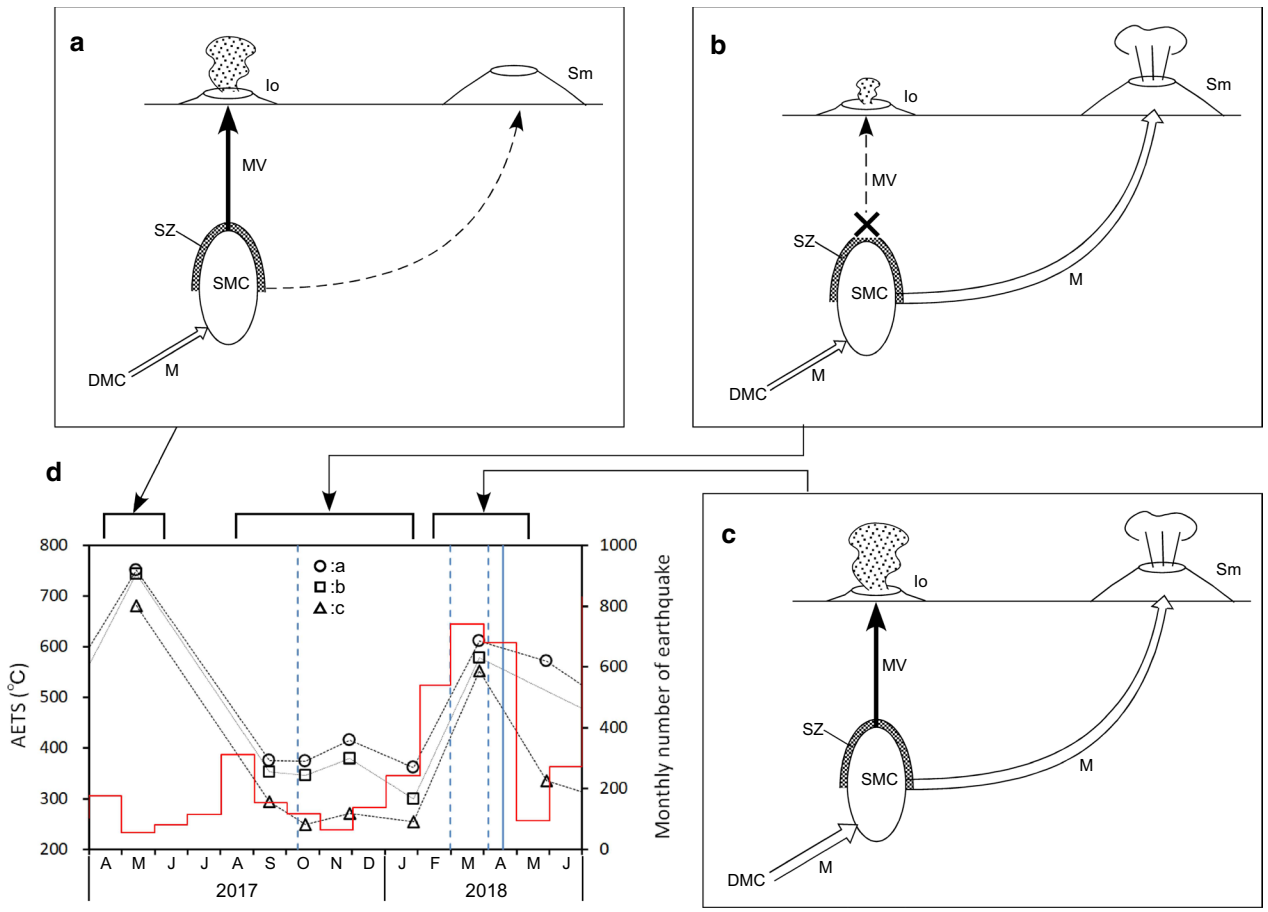

Fig. 7 Magma degassing and transport estimated from the correlation between changes in AETS and eruptions at Shinmoedake volcano (Sm). **a** Local situation in May 2017. A large flux of magmatic vapor (MV) was supplied to the aquifer beneath Ioyama volcano (Io). No magma was transported to Sm from the shallow magma chamber (SMC). The sealing zone (SZ) surrounding the SMC was open. **b** Local situation between September 2017 and January 2018. MV emission was prevented by SZ. Simultaneously, magma (M) was transported to Sm, causing a magmatic eruption. **c** Local situation between February and April 2018. A break in the SZ caused a large flux of MV to be supplied to Io. Magma was also transported to Sm. The flux of magma from the deep magma chamber (DMC) is likely to have increased from February to April 2018. **d** Changes in the apparent equilibrium temperature (AETS). Red histogram and vertical lines have the same meaning as in Fig. 3

$$\beta = \frac{C_{Lp}}{C_{Vp}} \tag{11}$$

where H, δ, and C represent enthalpy, isotope ratio in δ-notation, and the Ar/H_2O molar ratio, respectively. Ar/H_2O ratios are considered as a means to validate the model. In the above equations, f and g denote the mixing fraction of MV and the generating fraction of Vp, respectively. In general, g is not equal to f; their values are defined based on the amounts of H_2O in MV, LW, Vp, and Lp. Alpha (α) is the isotopic fractionation factor between Lp and Vp in terms of D/H and $^{18}O/^{16}O$ ratios and beta (β) is the distribution coefficient between Lp and Vp in terms of the Ar/H_2O ratio. Equations 7, 8, and 9 describe the conservation of enthalpy, isotopic ratio, and the amount of Ar, respectively. Equations 10 and 11 describe the equilibrium distribution between Vp and Lp in terms of stable isotopes and Ar, respectively. Using Eqs. 7–11, the isotopic ratios and Ar/H_2O ratios of Vp and Lp were calculated. The numerical values necessary for this calculation are listed in Table 2.

As shown in Fig. 9a, the calculated vapor phase lines at 100 °C and 160 °C (Vp-100 and Vp-160) are located near the point of the observed fumarole. Furthermore, Y1 is located between the calculated liquid phase lines at 100 °C and 160 °C (Lp-100 and Lp-160). These agreements suggest that MV and LW are mixed and that the phase-separated vapor phase (Vp) corresponds to fumarolic gas. The temperature of phase separation is estimated to be about 100–160 °C. To calculate the Vp and Lp lines in Fig. 9a,

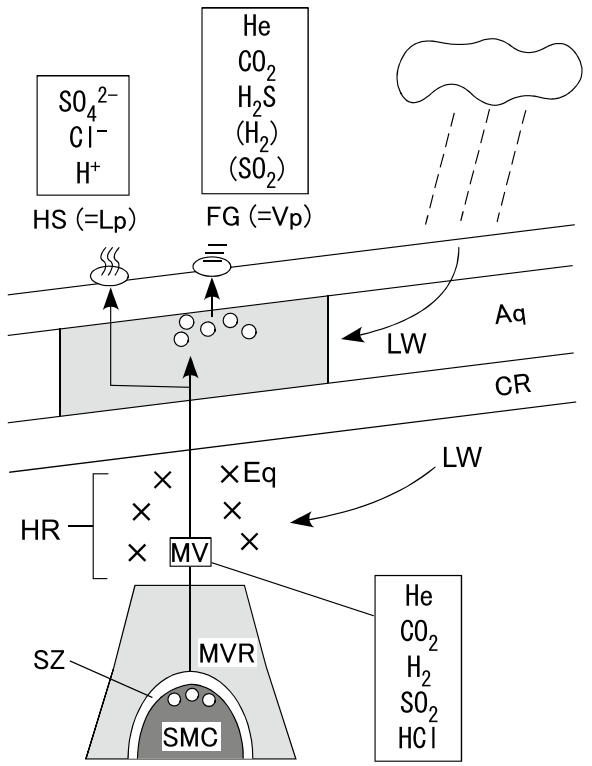

Fig. 8 Schematic illustration of local meteoric water (LW) in the shallow aquifer (Aq) beneath Iwoyama volcano interacting with magmatic vapor (MV). MV is discharged from the shallow magma chamber (SMH). MV moves up through the sealing zone (SZ), the magmatic vapor reservoir (MVR), and caprock (CR). MV produces volcanic earthquakes (Eq) in the region between MVR and CR. Interactions between MV and LW produce the vapor phase (*V*p) and the liquid phase (*L*p). A portion of both the *V*p and *L*p are discharged at the surface as fumarolic gas (FG) and hot spring water (HS), respectively. A portion of the SO_2 in MV is converted to SO_4^{2-} ion and H_2S gas, which are preferentially distributed to *L*p and *V*p, respectively

Table 2 Parameters for the calculation of the vapor and liquid phases

Term	Symbol	Value	Unit
Temp. of MV		900	℃
Temp. of LW		15	℃
Enthalpy of MV	HMV	4391	kJ/kg
Enthalpy of LW	HLW	64	kJ/kg
Enthalpy of Vp ditto			
At 100 ℃	HVp	2676	kJ/kg
At 160 ℃	HVp	2757	kJ/kg
Enthalpy of Lp ditto			
At 100 ℃	HLp	417	kJ/kg
At 160 ℃	HLp	677	kJ/kg
$\delta^{18}O$ of MV	δMV	− 8.0	‰
$\delta^{18}O$ of LW	δLW	− 8.2	‰
δD of MV	δMV	− 15.0	‰
δD of LW	δLW	− 53.5	‰
Ar/H_2O ratio of MV	CMV	0	
Ar/H_2O ratio of LW	CLW	3.0×10^{-7}	
$^{18}O/^{16}O$ fractionation factor	α	a	
D/H fractionation factor	α	a	
Ar/H_2O distribution coefficient	β	b	

a: Horita and Wesolowski (1994), b: Fermandez–Prini et al. (2003)

Enthalpy values are cited from the standard steam table (e.g., Japan Society of Mechanical Engineers 1999)

"f", which denotes the mixed fraction of MV, varied within the range of 0.10–0.6 at 100 °C. At 160 °C, "f" varied within the range of 0.15–0.6. If "f" has a value higher than these ranges, Lp is not formed, i.e., only Vp forms. If "f" has a value lower than these ranges, Vp is not formed; i.e., only Lp is formed. When "f" is fixed at its maximum, the isotope ratios of Vp and Lp are located at the right end of the Vp and Lp lines, respectively. When "f" is fixed at a minimum value, the isotope ratios of Vp and Lp are located at the left end of the Vp and Lp lines, respectively.

The highest $\delta^{18}O$ values were observed at fumarole "b" in March 2018. The "f" values producing the same $\delta^{18}O$ on the Vp line were 0.49 and 0.48, at 100 °C and 160 °C, respectively. The fumarolic δD and $\delta^{18}O$ increased rapidly during Period- I, and high values were maintained throughout Period- II (Fig. 5a, b). According to the above model for the formation of *V*p and *L*p, the increase in *V*p isotope ratios is due to an increase in the mixing ratio of MV. Therefore, the increase in the isotope ratios of H_2O denotes an increased flux of MV (under the assumption of a constant flux of LW).

Some fumarolic gases have isotopic ratios that are much lower than the *V*p line (Fig. 9a). When a part of H_2O in *V*p is condensed and lost, the isotopic ratio of the remaining water vapor decreases. This direction of change by condensation has the same direction as the vector connecting L and V-100 in Fig. 9a, i.e., the isotope ratios of liquid and vapor equilibrated at 100 °C. At the moment of condensation, the isotope ratio of the vapor phase leaves the *V*p line (*V*p-100 or 160) and moves toward the lower left. Some fumarolic gases with isotope ratios lower than the *V*p line can be explained by the partial condensation of water vapor (Ohba et al. 1997). Isotope ratios lower than the *V*p line can be also explained by the addition of water vapor generated from LW (Ohwada et al. 2003). In natural fumaroles, the above two effects may occur simultaneously. In Period-III, the low δD and $\delta^{18}O$ values can, therefore, be explained by the condensation of water vapor and or the influence of LW.

In Fig. 9b, the Ar/H_2O molar ratio of fumarolic gas is calibrated on the horizontal axis via conversion to the

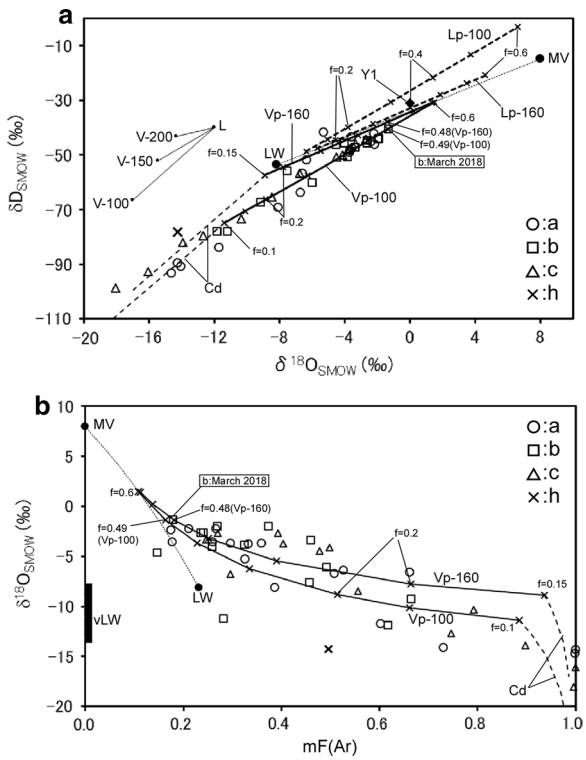

Fig. 9 **a** δD and $\delta^{18}O$ of H_2O in fumarolic gas with the calculated vapor phase (*V*p) and liquid phase (*L*p). Vp-100 and *V*p-160 denote *V*p of 100 °C and 160 °C, respectively. *L*p-100 and *L*p-160 denote *L*p at the temperature of 100 °C and 160 °C, respectively. The broken lines annotated as Cd indicate the isotopic ratio of remaining water vapor after partial condensation. V-100, 150 and 200 are the isotopic ratios of water vapor equilibrated with liquid L at 100 °C, 150 °C, and 200 °C, respectively. **b** Magnified Ar fraction, mF(Ar), and $\delta^{18}O$ of H_2O in fumarolic gases with *V*p-100 and *V*p-160. vLW indicates the vapor phase generated from local meteoric water (LW)

magnified Ar fraction in the Ar–H_2O binary system, which is defined as follows:

$$mF(Ar) = \frac{10^6\left(\frac{Ar}{H_2O}\right)}{10^6\left(\frac{Ar}{H_2O}\right)+1} \quad (12)$$

As shown in Fig. 9b, even for the relationship between mF(Ar) and $\delta^{18}O$, the calculated *V*p curves at 100 °C or 160 °C (i.e., *V*p-100 or *V*p-160) are closely linked to fumarolic gases. The increased atmospheric contamination drives the points to the right in the diagram. Fumarolic gases with $\delta^{18}O$ higher than that of the *V*p-160 curve are interpreted to have suffered the contamination by an atmospheric component. Fumarolic gases located beneath the Vp-100 curve are considered to have been affected by the partial condensation of water vapor and the addition of water vapor originating in meteoric water (vLW in Fig. 9b). The Vp curve overlaps with the isotopic ratios of fumarolic gases, especially in the low mF(Ar) and high $\delta^{18}O$ region, indicating the validity of the *V*p and *L*p formation model.

In the above model, mixing between LW and MV occurs during a single stage, but, as shown in Fig. 8, mixing can occur at both the HR located under the caprock and in the aquifer. It is not possible to evaluate the relative contributions of these two mixing events based solely on the isotope ratio of fumarolic gases.

Correlation between concentrations of gaseous species

Examining the correlation among the concentrations of species in fumarolic gases is useful for estimating the origin of each species, as well as for estimating the state of the hydrothermal system. In the He–N_2–Ar ternary system (Fig. 10a), it has been reported that a mixing relationship holds between two end members, i.e., magmatic and atmospheric components (Kita et al. 1993; Giggenbach 1997; Taran 2011; Ohba et al. 2019a, b). In this study, we also found that the composition of fumarolic gas was distributed between these two endmembers (Fig. 10a). The magmatic endmember (broken circle) has a fixed N_2/He ratio and is poor in Ar. The atmospheric endmember is composed of air and the component dissolved in water saturated with air (ASW).

In the He–N_2–CO_2 ternary system (Fig. 10b), the fumarolic gases are concentrated almost into a single group (broken circle in Fig. 10b). Since helium is a magmatic component, the grouping in the He–N_2–CO_2 ternary system suggests that CO_2 is also a magmatic component. Some points are distributed in the direction of the angle of N_2 away from the group. Their distribution indicates contamination by atmospheric components.

In the He–N_2–CH_4 ternary system, fumarolic gases can be divided into two groups, although the distance between these groups is small (Fig. 10c). Some points distributed near the N_2 corner indicate the contamination by atmospheric components. According to Fig. 11a, the CH_4/He ratio is low during the latter half of Period-II, when eruptions occurred at the Shinmoedake and Ioyama volcanoes. At Periods-I and -III, the CH_4/He ratio is generally high. The distribution of fumarolic gases in Fig. 10c suggests that CH_4 is essentially a magmatic component (broken circle). In addition to magmatic CH_4, non-magmatic CH_4 component was observed; this is deemed to be contaminative. For non-magmatic CH_4, a thermogenic origin is possible, i.e., generation via the decomposition of organic matter in the crust.

Based on the SO_2–CO_2–H_2S ternary system, the type of the hydrothermal system can be estimated. According to Stix and de Moor (2018), a hydrothermal system with deep-seated degassing magma can be distinguished from

a hydrothermal system with a shallowly intruded degassing magma by the SO_2–CO_2–H_2S ternary composition of fumarolic gas. In addition to this distinguishment, the SO_2–CO_2–H_2S ternary system enables the evaluation of interaction between MV and shallow aquifer. The observed CO_2/St ratio (where St refers to the molar summation of SO_2 and H_2S) of fumarolic gases are distributed in a large range (between 1.4 and 22) (Fig. 10d). Most fumarolic gases have H_2S/SO_2 molar ratios greater than 4; such gases are located in the region considered to be hydrothermally dominated (HD; Fig. 10d). As shown in Fig. 11b, all fumarolic gases measured during Period-I are classified as HD-type. Some fumarolic gases with low H_2S/SO_2 ratios are classified as hydrothermal magmatic types. Furthermore, the hydrothermal magmatic types can be divided into deep hydrothermal magmatic (DHM) and shallow

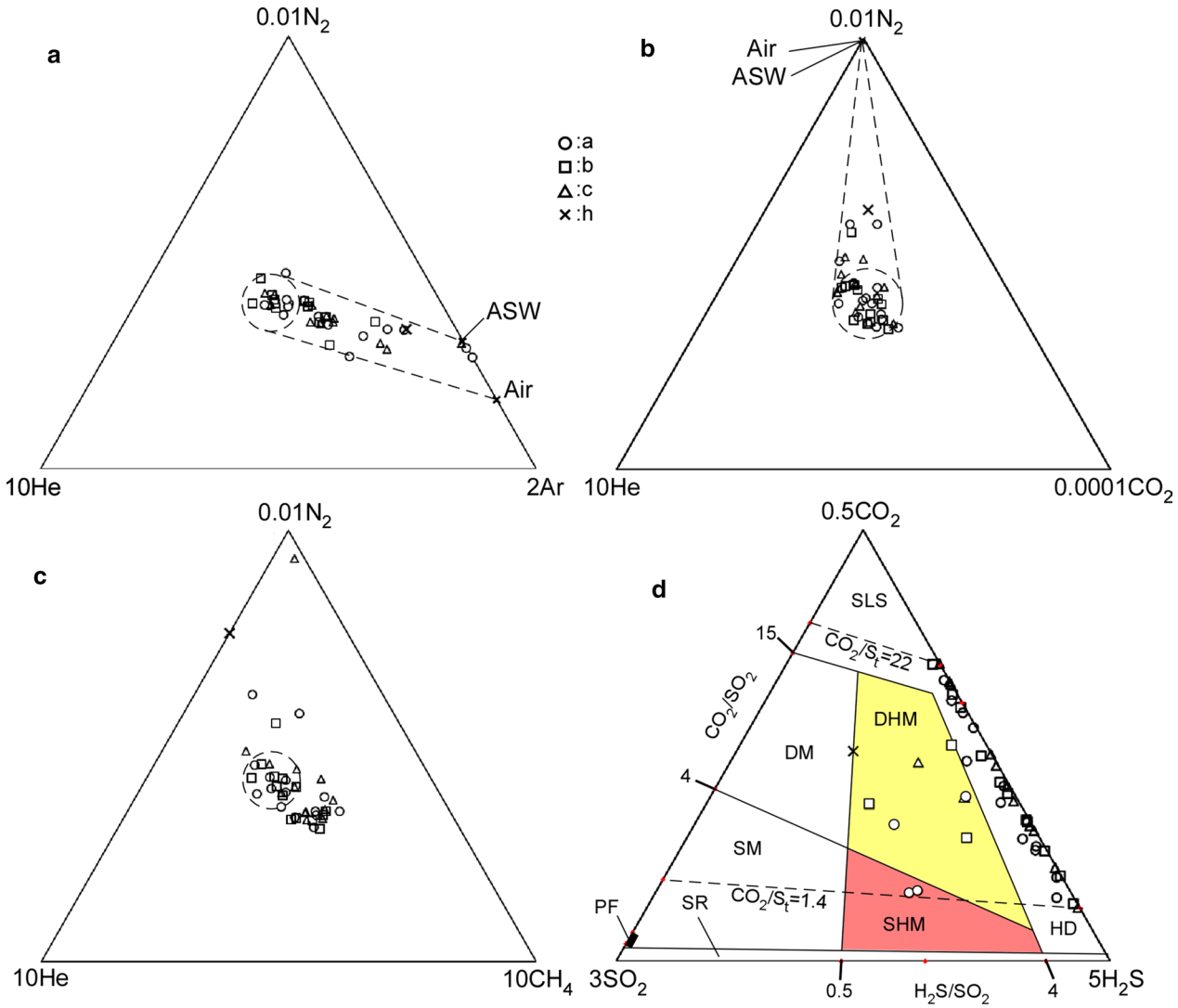

Fig. 10 **a** Fumarolic gas compositions in the He–N_2–Ar ternary system; broken circle indicates the expected magmatic end member. ASW is the composition of air dissolved in water. Broken lines indicate the mixing between the magmatic and atmospheric end members. **b** Fumarolic gas compositions in the He–N_2–CO_2 ternary system; broken circle indicates the expected magmatic end member. Broken lines indicate the mixing between the magmatic and atmospheric end members. **c** Fumarolic gas composition in the He–N_2–CH_4 ternary system; broken circle indicates the expected magmatic end member. **d** Fumarolic gas composition in the SO_2–CO_2–H_2S ternary system classified as a hydrothermal system (Stix and de Moor 2018). SLS, HD, DHM, SHM, DM, SM and SR indicate the types of volcanic gas with the following geneses: "S loss scrubbing", "hydrothermally dominated", "deep hydrothermal-magmatic", "shallow hydrothermal-magmatic", "deep magmatic", "shallow magmatic" and "sulfur remobilization", respectively. PF indicates the estimated parental magmatic fluid in the Kirishima volcanic area (Ohba et al. 1997). The CO_2/SO_2 and H_2S/SO_2 molar ratios are calibrated on the left and bottom sides, respectively. The CO_2/St isomolar ratio is indicated by broken lines where St is the summation of SO_2 and H_2S

hydrothermal magmatic (SHM) based on their CO_2/SO_2 ratios. Fumarolic gases of the DHM type were observed during Periods-II and -III (yellow circles in Fig. 11b), whereas SHM gases were observed only observed during Period-II (red circles in Fig. 11b). The fumarolic gas "a" observed in May 2017 and March 2018 is classified into the SHM field, with a CO_2/SO_2 ratio less than 4. The AETS of these two fumarolic gases were calculated as 752 °C and 611 °C (Fig. 6a), suggesting an increased MV flux in both May 2017 and March 2018. Therefore, the discharge of SHM-type fumarolic gases is regarded as an index for enhanced volcanic activity at Ioyama volcano.

PF in Fig. 10d shows the composition of the parental fluid released from the magma of Kirishima volcano. The CO_2/St of PF was estimated at 0.25–0.44 (Ohba et al 1997). In Fig. 10d, the sulfur component in PF is considered to be SO_2. The CO_2/St ratio of fumarolic gases (1.4–22) is higher than the CO_2/St ratio of PF. If the essential CO_2/St ratio of MV is similar to the CO_2/St ratio of PF, it means that MV loses sulfur-bearing gases during travel to the surface. As suggested in the previous section, fumarolic gases was comprised of the vapor phase formed during the interaction of MV and LW. The following hydrolysis reaction is expected to occur during this interaction (Kusakabe et al. 2000):

$$4SO_2 + 4H_2O = 3HSO_4^- + H_2S + 3H^+ \quad (13)$$

Through the above reaction, some SO_2 in MV is absorbed by LW in the form of the SO_4^{2-} ion. Indeed, near the fumaroles of Ioyama volcano, hot spring waters rich in SO_4^{2-}, such as K3 and Y1, were discharged (Tajima et al 2020). In addition, MV can be depleted in sulfur species through other reactions (e.g., Takano et al. 2004), such as

$$SO_2 + 3H_2S = 3S + 2H_2O \quad (14)$$

The absorption of SO_2 by LW and the formation of native sulfur can explain the depletion of St in fumarolic gases relative to PF (Fig. 10d). Unlike SO_2, CO_2 in MV is not readily dissolved in Lp; thus, most of the constituent CO_2 is distributed to *V*p. Consequently, the CO_2/SO_2 ratio of fumarolic gases reflects the degree of SO_2 removal.

Conclusions

This study has reported direct sampling and analysis of fumarolic gas at Ioyama volcano between December 2015 and July 2020. Notable changes in the chemical composition related to volcanic activity included increased concentrations of SO_2 and H_2 in May 2017

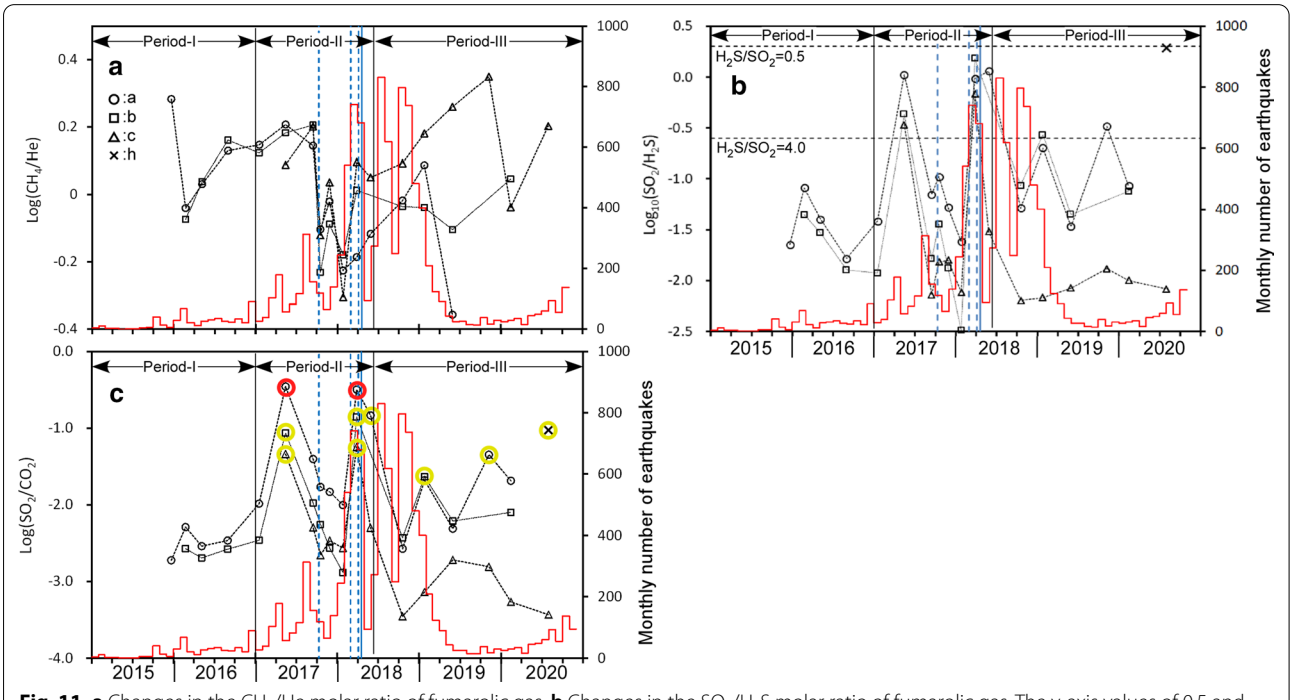

Fig. 11 **a** Changes in the CH_4/He molar ratio of fumarolic gas. **b** Changes in the SO_2/H_2S molar ratio of fumarolic gas. The y-axis values of 0.5 and 4 for H_2S/SO_2 ratio were indicated by the two horizontal broken lines. **c** Changes in the SO_2/CO_2 molar ratio of fumarolic gas. Fumarolic gases surrounded by red and yellow circles are classified as being of shallow hydrothermal magmatic (SHM) and deep hydrothermal magmatic (DHM) origins, respectively. Red histogram and vertical lines are the same as in Fig. 3

and March 2018. Sampling in March 2018 took place immediately before the eruption at Ioyama volcano in April 2018. Based on the isotope ratio of H_2O in fumarolic gas, the observation period was divided into three periods: Period-1 (December 2015 to December 2016), Period-II (January 2017 to May 2018), and Period-III (June 2018 to July 2020). Using their SO_2–CO_2–H_2S ternary composition, most collected fumarolic gases were classified as HD. In particular, for Period-I, all fumarolic gases were classified as HD. During Period-II, SHM and DHM were observed in addition to HD gas. Period-III featured DHM- and HD-type gases. The fumarolic gas released in March 2018 was classified as SHM-type, and furthermore, its AETS was high. Therefore, the shift of composition to the SHM-type as well as rise of AETS would be good precursors of phreatic eruptions, because they are related to a large flux of MV.

Correlating changes in AETS with the occurrence of eruptions at Shinmoedake volcano, the occurrence of magma sealing and transport was estimated as follows. In May 2017 and in March 2018, the AETS of fumarolic gas increased, suggesting an increased MV flux. Between September 2017 and January 2018, AETS decreased, suggesting a reduced MV flux, probably due the magma sealing in SMC. Simultaneously with this decrease in AETS, magmatic eruptions occurred at Shinmoedake volcano, suggesting magma transport from the chamber to Shinmoedake volcano. It is noticeable that magma sealing and displacement of magma happened simultaneously.

Interactions between MV and LW in aquifers generated a vapor phase (*V*p) and coexisting liquid phase (*L*p). A portion of *V*p was released as fumarolic gas, whereas a portion of *L*p was discharged as acidic hot spring waters enriched in the SO_4^{2-} ion. The temperatures of *V*p and *L*p were estimated to be 100–160 °C. Based on the isotopic ratio of H_2O, the maximum mixing fraction of MV was estimated at 0.49. Comparing the CO_2/SO_2 ratios of fumarolic gas with an estimated essential CO_2/SO_2 ratio of MV, the former was found to be significantly higher than the latter. The following phenomena are considered likely cause for this observation. Although much SO_2 in MV was converted to $SO_4^{2-}$and H_2S by interaction with LW, CO_2 did not undergo a similar reaction and was distributed to the vapor phase. The low CO_2/SO_2 ratio of fumarolic gas immediately prior to the eruption at Ioyama volcano suggests limited interaction between MV and LW, and thus, fumarolic gas sustained the magmatic features observed.

Abbreviations

AETS: Apparent equilibrium temperature defined for the reaction including sulfur species; AETD: Apparent equilibrium temperature defined for the deuterium exchange reaction between H_2O and H_2; AMW: Andesitic magma water; ASW: Atmospheric components saturated in water; JMA: Japan Meteorological Agency; Lp: Liquid phase; LW: Local meteoric water; MV: Magmatic vapor; MT: Magnetotelluric; R-gas: Residual gas; SMOW: Standard mean ocean water; St: Molar summation of SO_2 and H_2S; vLW: Vapor generated from LW; VEI: Volcanic Explosivity Index; Vp: Vapor phase.

Acknowledgements

We would like to thank Dr. M de Moor and one anonymous reviewer for their constructive comments to the manuscript, by which the content of this paper was significantly improved. We also thank Dr. T Fischer for his editorial handling of the manuscript.

Authors' contributions

TO drafted the manuscript. YM sampled fumarolic gases and analyzed them. UT, MI and RS analyzed the fumarolic gas samples. All the authors read and approved the final manuscript.

Funding

This work was supported by the Japanese Ministry of Education, Culture, Sorts, Science and Technology under grant of the Integrated Program for Next Generation Volcano Research and Human Resource Development in 2016–2020. This study was partially funded by Earthquake Res., Inst., the University of Tokyo, Joint Research program 2020-KOBO11.
This work was also partially supported by JSPS KAKENHI Grant Number JP16777378, JP18058728, JP19209043, and JP20298572.

Availability of data and materials

The csv files for Table 1 will be stored in repositories.

Declarations

Ethics approval and consent to participate

Not applicable.

Consent for publication

Not applicable.

Competing interests

The authors declare that they have no competing interests.

Author details

[1] Tokai University, 4-1-1 Kitakaname Hiratsuka, Kanagawa 259-1291, Japan. [2] Meteorological Research Institute, 1-1 Nagamine Tsukuba, Ibaraki 305-0052, Japan. [3] Graduate School of Environmental Studies, Nagoya University, Furo-cho, Chikusa-ku, Nagoya 464-8601, Japan.

Received: 12 January 2021 Accepted: 24 March 2021
Published online: 31 March 2021

References

Aizawa K, Koyama T, Hase H, Uyeshima M, Kanda W, Utsugi M, Yoshimura R, Yamaya Y, Hashimoto T, Yamazaki K, Komatsu S, Watanabe A, Miyakawa K, Ogawa Y (2014) Three-dimensional resistivity structure and magma plumbing system of the Kirishima Volcanoes as inferred from broadband magnetotelluric data. J Geophys Res Solid Earth 119:198–215. https://doi.org/10.1002/2013JB010682

Barberi F, Bertagnini A, Landi P, Principe C (1992) A review on phreatic eruptions and their precursors. J Volcanol Geotherm Res 52:231–324

Chiodini G, Caliro S, Cardellini C, Granieri D, Avino R, Baldini A, Donnini M, Minopoli C (2010) Long-term variations of the Campi Flegrei, Italy, volcanic system as revealed by the monitoring of hydrothermal activity. J Geophys Res 115:B03205. https://doi.org/10.1029/2008JB006258

Fernández-Prini R, Alvarez JL, Harvey AH (2003) Henry's constants and vapor-liquid distribution constants for gaseous solutes in H_2O and D_2O at high temperatures. J Phys Chem Ref Data 32:903–916

Fischer TP, Ramírez C, Mora-Amador RA, Hilton DR, Barnes JD, Sharp ZD, Le Brun M, de Moor JM, Barry PH, Füri E, Shaw AM (2015) Temporal variations in fumarole gas chemistry at Poás volcano, Costa Rica. J Volcanol Geotherm Res 294:56–70

Fournier RO (1999) Hydrothermal processes related to movement of fluid from plastic into brittle rock in the magmatic-epithermal environment. Econ Geol 94:1193–1211
Funasaki J, Shimomura M, Kuroki C (2017) Document on Geothermal Activities at Ebino Highland including Iou-yama, Kirishima Volcano, since the Meiji era. Quarterly J Seismol 80:1–11
Giggenbach WF (1975) A simple method for the collection and analysis of volcanic gas samples. Bull Volcanol 39:132–145
Giggenbach WF (1987) Redox processes governing the chemistry of fumarolic gas discharges from White Island, New Zealand. Appl Geochem 2:143–161
Giggenbach WF (1992) Isotopic shifts in waters from geothermal and volcanic systems along convergent plate boundaries and their origin. Earth Planet Sci Lett 113:495–510
Giggenbach WF (1997) The origin and evolution of fluids in magmatic-hydrothermal systems. In: Barnes HL (ed) Geochemistry of hydrothermal ore deposits, 3rd edn. Wiley, New York
Horita J, Wesolowski DJ (1994) Liquid-vapor fractionation of oxygen and hydrogen isotopes of water from the freezing to the critical temperature. Geochim Cosmochim Acta 58:3425–3437
Imura R, Kobayashi T (2001) Geological map of Kirishima volcano. Geological Survey of Japan.
Japan Meteorological Agency (2020a) https://www.data.jma.go.jp/svd/vois/data/tokyo/305_Kusatsu-Shiranesan/305_index.html. Accessed 24 Dec 2020.
Japan Meteorological Agency (2020b) https://www.data.jma.go.jp/svd/vois/data/fukuoka/505_Kirishimayama/505_index.html. Accessed 23 Dec 2020.
Japan Society of Mechanical Engineers (1999) Steam tables, 5th edn. Japan Society of Mechanical Engineers, Tokyo
Kagiyama T, Uhira K, Watanabe T, Masutani F, Yamaguchi M (1979) Geothermal survey of the volcanoes Kirishima. Bull Earthquake Res Inst Univ Tokyo 54:187–210
Kita I, Nitta K, Nagao K, Taguchi S, Koga A (1993) Difference in N_2/Ar ratio of magmatic gases from northeast and southwest Japan: new evidence for different states of plate subduction. Geology 21:391–394
Kusakabe M, Komoda Y, Takano B, Abiko T (2000) Sulfur isotopic effects in the disproportionation reaction of sulfur dioxide in hydrothermal fluids: implications for the δ34S variations of dissolved bisulfate and elemental sulfur from active crater lakes. J Volcanol Geotherm Res 97:287–307
Lee S, Ohba T, Yun SH, Yang K, Jeong HY (2016) Evaluation of sampling methods for sulfur speciation in volcanic gases. Chem Geol 438:123–133
Nakada S, Magai M, Kaneko T, Suzuki Y, Maeno F (2013) The outline of the 2011 eruption at Shinmoe-dake (Kirishima), Japan. Earth Planets Space 65:475–488. https://doi.org/10.5047/eps.2013.03.001
Ohba T, Hirabayashi J, Yoshida M (1994) Equilibrium temperature and redox state of volcanic gas at Unzen volcano, Japan. J Volcanol Geotherm Res 60:263–272
Ohba T, Nogami K, Hirabayashi J (1997) Hydrothermal system of Kirishima volcanic area inferred from the chemical and isotopic composition of spring waters and fumarolic gases. Bull Volcanol Soc Japan 42:1–15
Ohba T, Nogami K, Hirabayashi J, Sawa T, Kazahaya K, Morikawa N, Ohwada M (2011) Chemical and isotopic composition of fumarolic gases at Iwate volcano, Japan, during and after seismic activity in 1998: implications for the modification of ascending volcanic gases. Annals Geophy 54:187–197. https://doi.org/10.4401/ag-5182
Ohba T, Yaguchi M, Nishino K, Numanami N, Tsunogai U, Ito M, Shingubara R (2019) Time variation in the chemical and Isotopic composition of fumarolic gasses at Kusatsu-Shirane Volcano. Jpn Front Earth Sci 7:249. https://doi.org/10.3389/feart.2019.00249
Ohba T, Yaguchi M, Nishino K, Numanami N, Daita Y, Sukigara C, Ito M, Tsunogai U (2019) Time variations in the chemical and isotopic composition of fumarolic gases at Hakone volcano, Honshu Island, Japan, over the earthquake swarm and eruption in 2015, interpreted by magma sealing model. Earth Planets Space 71:48. https://doi.org/10.1186/s40623-019-1027-5
Ohwada M, Ohba T, Hirabayashi J, Nogami K, Nakamura K, Nagao K (2003) Interaction between magmatic fluid and meteoric water, inferred from $^{18}O/^{16}O$ and $^{36}Ar/H_2O$ ratios of fumarolic gases at the Kusatsu Shirane volcano, Japan. Earth Planets Space 55:105–110. https://doi.org/10.1186/BF03351737
Oikawa T, Yoshimoto M, Nakada S, Maeno F, Komori J, Shimano T, Takeshita Y, Ishizuka Y, Ishimine Y (2016) Reconstruction of the 2014 eruption sequence of Ontake Volcano from recorded images and interviews. Earth Planets Space 68:79. https://doi.org/10.1186/s40623-016-0458-5
Ossaka J, Ozawa T, Nomura T, Ossaka T, Hirabayashi J, Takaesu A, Hayashi T (1980) Variation of chemical compositions in volcanic gases and waters at Kusatsu-Shirane Volcano and its activity in 1976. Bull Volcanol 43:207–216
Ozawa T (1968) Chemical analysis of volcanic gases: I. Chemical analysis of volcanic gases containing water vapor, hydrogen chloride, sulfur dioxide, hydrogen sulfide, carbon dioxide, etc. Geochem Int 5:939–947
Richet P, Bottinga Y, Javoy M (1977) A review of hydrogen, carbon, nitrogen, oxygen, sulphur, and chlorine stable isotope fractionation among gaseous molecules. Ann Rev Earth Planet Sci 5:65–110
Stix J, de Moor J, Maarten, (2018) Understanding and forecasting phreatic eruptions driven by magmatic degassing. Earth Planets Space 70:83. https://doi.org/10.1186/s40623-018-0855-z
Tajima Y, Nakada S, Maeno F, Huruzono T, Takahashi M, Inamura A, Matsushima T, Nagai M, Funasaki J (2020) Shallow magmatic hydrothermal eruption in April 2018 on Ebinokogen Ioyama volcano in Kirishima volcano group, Kyushu. Jpn Geosci 10:183. https://doi.org/10.3390/geosciences10050183
Takano B, Suzuki K, Sugimori K, Ohba T, Fazlullin SM, Bernard A, Sumarti S, Sukhyarg R, Hirabayashi M (2004) Bathymetric and geochemical investigation of Kawah Ijen crater lake, east Java, Indonesia. J Volcanol Geotherm Res 135:299–329
Taran Y (2011) N_2, Ar, and He as a tool for discriminating sources of volcanic fluids with application to Vulcano, Italy. Bull Volcanol 73:395–408
Taran YA, Pokrovsky BG, Dubik YM (1989) Isotopic composition and origin of water from andesitic magmas. Dokl Acad Nauk USSR 304:440–443
Taran Y, Gavilanes JC, Cortes A (2002) Chemical and isotopic composition of fumarolic gases and the SO_2 flux from Volcan de Colima, Mexico, between the 1994 and 1998 eruptions. J Volcanol Geotherm Res 117:105–119
Tassi F, Vaselli O, Capaccioni B, Macias JL, Nencetti A, Montegrossi G, Magro G (2003) Chemical composition of fumarolic gases and spring discharges from El Chicho'n volcano, Mexico: causes and implications of the changes detected over the period 1998–2000. J Volcanol Geotherm Res 123:105–121
Tsunogai U, Kamimura K, Anzai S, Nakagawa F, Komatsu D (2011) Hydrogen isotopes in volcanic plumes: tracers for remote temperature sensing of fumaroles. Geochim Cosmochim Acta 75:4531–4546
Utada H, Kagiyama T, EM Research Group for Kirishima volcano (1994) Deep resistivity structure of Kirishima volcano (I). Bull Earthq Res Inst Univ Tokyo 69:241–255

Publisher's Note